

Distinguishing Ordered Phases using Machine Learning and Classical Shadows

Leandro Morais,^{1,2} Tiago Pernambuco,³ Rodrigo G. Pereira,^{1,3}
Askery Canabarro,^{4,5} Diogo O. Soares-Pinto,² and Rafael Chaves^{1,6}

¹*International Institute of Physics, Federal University of Rio Grande do Norte, 59078-970 Natal, Brazil*

²*Instituto de Física de São Carlos, Universidade de São Paulo, CP 369, 13560-970 São Carlos, SP, Brazil*

³*Departamento de Física Teórica e Experimental, Universidade Federal do Rio Grande do Norte, 59078-970 Natal-RN, Brazil*

⁴*Grupo de Física da Matéria Condensada, Núcleo de Ciências Exatas - NCEX,*

Campus Arapiraca, Universidade Federal de Alagoas, 57309-005 Arapiraca-AL, Brazil

⁵*Quantum Research Center, Technology Innovation Institute, Abu Dhabi, UAE*

⁶*School of Science and Technology, Federal University of Rio Grande do Norte, 59078-970 Natal, Brazil*

(Dated: January 30, 2025)

Classifying phase transitions is a fundamental and complex challenge in condensed matter physics. This work proposes a framework for identifying quantum phase transitions by combining classical shadows with unsupervised machine learning. We use the axial next-nearest neighbor Ising model as our benchmark and extend the analysis to the Kitaev-Heisenberg model on a two-leg ladder. Even with few qubits, we can effectively distinguish between the different phases of the Hamiltonian models. Moreover, given that we only rely on two-point correlator functions, the classical shadows protocol enables the cost of the analysis to scale logarithmically with the number of qubits, making our approach a scalable and efficient way to study phase transitions in many-body systems.

I. INTRODUCTION

Machine learning (ML) techniques have recently attracted considerable attention for their applications in quantum many-body physics [1–5]. One particularly promising area is their capability to distinguish between different phases and identify phase transitions across a range of Hamiltonian models [6–13]. Traditional approaches, such as calculating order parameters and correlation functions, often face significant challenges in high-dimensional systems and may become impractical. Additionally, these methods are limited when dealing with systems exhibiting topological order, where phase transitions are not easily characterized by standard observables, cases in which alternative metrics, such as the Chebyshev distance, have shown greater effectiveness [14]. By uncovering subtle patterns in quantum many-body data that indicate phase transitions, ML is proving instrumental in overcoming these limitations, offering new insights into complex quantum systems.

Despite significant advancements, ML methods remain heavily reliant on high-quality input data, and generating such data for quantum many-body systems is a formidable challenge due to the exponential growth of the Hilbert space with increasing system size. Classical computational techniques, such as quantum Monte Carlo simulations [15] and matrix product state (MPS) tomography [16], have achieved notable success but often struggle with the complexity and diversity of these systems. In turn, fault-tolerant quantum computers present a promising alternative by enabling more efficient simulations of quantum many-

body systems, potentially improving data availability for ML models. These quantum devices leverage variational quantum methods to prepare ground states of Hamiltonians and quantum machine learning (QML) techniques to analyze information about these states. However, realizing this potential quantum advantage is hindered by significant theoretical and practical challenges, including barren plateaus and local minima, which complicate the training of variational algorithms [17, 18]. A pragmatic solution involves integrating quantum-generated data with classical algorithms, exploiting the strengths of classical machine learning to tackle problems beyond classical computational limits and, in some cases, rival QML models [19]. Nonetheless, fully characterizing quantum systems remains constrained by the need for exponentially increasing measurements as the number of qubits grows.

Recent breakthroughs offer a promising approach to mitigate this measurement bottleneck. As demonstrated by Aaronson [20], much of the data traditionally deemed necessary for predicting certain properties of quantum systems is, in fact, redundant. This insight led to the development of the classical shadows protocol, a method that enables accurate predictions of both linear and nonlinear functions of quantum systems with substantially fewer measurements, all while maintaining controlled error margins [5]. By significantly reducing the measurement overhead, classical shadows provide a powerful tool for overcoming the curse of dimensionality, making them invaluable for exploring quantum phases and facilitating ML applications in complex quantum

systems.

In this work, we employ classical shadow techniques to efficiently estimate expectation values and classify the phases of two paradigmatic spin-1/2 chain models: the axial next-nearest neighbor Ising (ANNNI) model [21] and the Kitaev-Heisenberg ladder [22]. Both models are relevant for describing the magnetic properties of real materials and display rich phase diagrams with multiple ordered and disordered phases. The ANNNI model is significant as the simplest model in which different types of competing magnetic orders stem from the interplay between frustrated Ising interactions and quantum fluctuations induced by a transverse magnetic field. In turn, in the Kitaev-Heisenberg ladder, the regime of dominant bond-dependent Kitaev interactions harbors two Kitaev spin liquid (KSL) phases, which can be viewed as topological phases characterized by gapped Majorana fermion excitations [23], a nonlocal string order parameter, and double degeneracy of the entanglement spectrum [22]. Distinguishing these KSL phases from the long-range ordered and disordered phases that emerge when Heisenberg interactions perturb the pure Kitaev model is a crucial challenge in the search for exotic magnetic states in low-dimensional systems [24].

Using randomized measurements, we efficiently generate data sets for both models, which are subsequently analyzed using the KMeans algorithm [25], an unsupervised machine learning method for clustering and classification. Our results demonstrate that this approach is highly effective in distinguishing between different quantum phases, even for small system sizes.

The paper is organized as follows. In Sec. II, we introduce the Hamiltonian analyzed in this paper, where we discuss the ANNNI and Kitaev-Heisenberg models. Next, we provide an overview of classical shadows in Sec. III and explain the ML pipeline for the different models. Then, in Sec. V, we present the results of machine learning phase transitions, including the model outcomes. Finally, we conclude with a discussion of our findings in Sec. VI.

II. HAMILTONIAN MODELS

To demonstrate the effectiveness of classical shadows in generating data for phase distinction in many-body systems, we examine two Hamiltonian models with paradigmatic features: the ANNNI model [26–32] and the Kitaev-Heisenberg model [22, 33–37]. Details of these models are provided below.

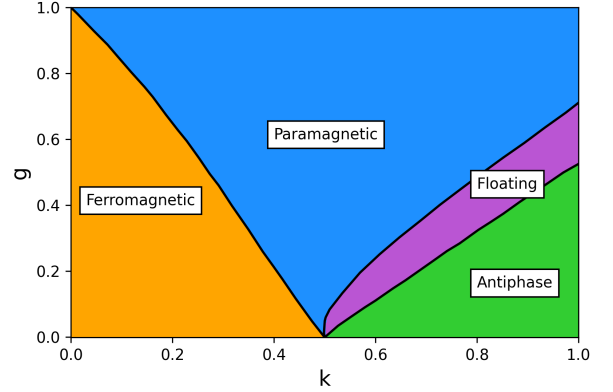


FIG. 1. Phase diagram for the ANNNI chain. Phase transition lines were constructed based on [38].

A. THE ANNNI MODEL

The ANNNI model was originally proposed to explain the magnetic ordering properties of rare-earth metals [26]. The Hamiltonian for a one-dimensional chain is given by

$$H = -J_1 \sum_i S_i^z S_{i+1}^z + J_2 \sum_i S_i^z S_{i+2}^z - h \sum_i S_i^x, \quad (1)$$

where S_i^α with $\alpha = x, y, z$ are spin- $\frac{1}{2}$ operators at site i , $J_1 > 0$ describes a ferromagnetic Ising interaction between spins on nearest-neighbor (NN) sites, $J_2 > 0$ corresponds to a next-nearest-neighbor (NNN) antiferromagnetic interaction and the last term accounts for a transverse field acting on every lattice site.

Despite its relative simplicity, the ANNNI model exhibits a complex phase diagram as the relative transverse field strength, $g = h/J_1$, and the ratio between NN and NNN interaction strengths, $k = J_2/J_1$, are varied. This model is significant because it is the simplest system that combines the effects of quantum fluctuations—induced by the transverse field—and competing, frustrated exchange interactions. This interplay results in a rich ground-state phase diagram that has been studied extensively through analytical and numerical methods [27–32]. It consists of four distinct phases [39, 40]:

1. For small k and g , the system is in the ferromagnetic phase. In this phase, the system spontaneously breaks the \mathbb{Z}_2 symmetry $\sigma_j^z \mapsto -\sigma_j^z$. The two degenerate ground states are adiabatically connected to the product states in which the spins order themselves either as $\uparrow\uparrow \dots \uparrow\uparrow$ or as $\downarrow\downarrow \dots \downarrow\downarrow$;

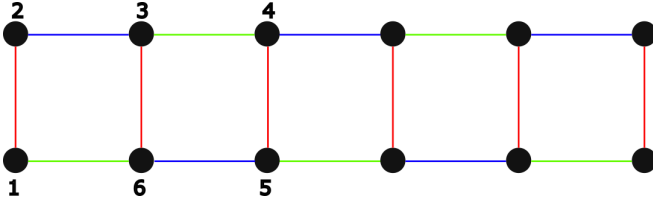


FIG. 2. The Kitaev-Heisenberg ladder. Blue, green and red lines indicate $\gamma = x, y$ and z couplings respectively. The numbered sites on the ladder define the unit cell on which the plaquette operator in Eq. (4) is to be computed.

2. For large enough g , the transverse field term dominates and the system enters a paramagnetic disordered phase, with a unique ground state of spins aligned with the field;
3. For large k , we have the so-called "antiphase", where the strong antiferromagnetic coupling between NNN spins causes the system to order with the pattern $\uparrow\uparrow\downarrow\downarrow\uparrow\uparrow \dots$, breaking the \mathbb{Z}_2 symmetry as well as translation invariance. The ground state is fourfold degenerate;
4. For a small region of intermediate k and g , the system is in a gapless "floating phase" with power-law-decaying correlations.

The phase diagram of the ANNNI chain as a function of k and g is shown in Fig. 1.

The ANNNI model has a wide range of practical applications, including the description of rare-earth metals [26, 39], the explanation of magnetic ordering in certain quasi-one-dimensional spin ladder materials [41], the study of dynamical phase transitions [42], and the exploration of interactions between Majorana edge modes in arrays of Kitaev chains [43, 44]. These diverse applications make it a paradigmatic model in many-body physics.

Building on the results in [45, 46], we will use the two-point correlation functions between all spins in the chain as input for the ML model. Unlike [45, 46], which relied on the diagonalization of the Hamiltonian, we will use classical shadows to estimate these expectation values in a much more efficient manner.

B. THE KITAEV-HEISENBERG MODEL

Quantum spin liquids are among the most fascinating topics in contemporary condensed matter physics [47, 48], particularly since the introduction of the exactly solvable Kitaev model on a honeycomb lattice [33], which hosts a phase known as the KSL. These KSL phases are of great interest due to their unique properties: when subjected to a magnetic field,

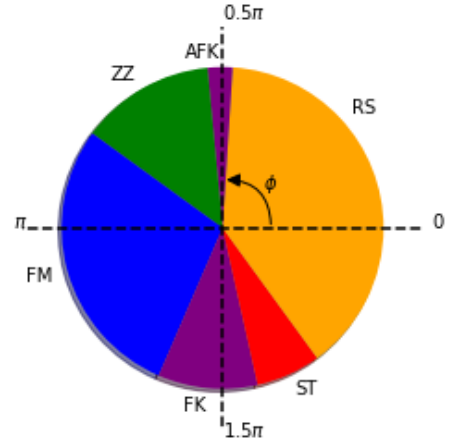


FIG. 3. Phase diagram of the Kitaev-Heisenberg model as a function of the parameter ϕ . The boundaries between the phases were calculated in Refs. [22] and [49].

they exhibit non-abelian anyonic excitations in the form of Ising anyons [33, 34]. These excitations are particularly noteworthy because, in theory, they could be utilized for fault-tolerant quantum computation [35].

Realistic models for candidate Kitaev materials, however, usually include perturbations beyond the exactly solvable model, for instance Heisenberg exchange interactions, which drive a wealth of magnetic orders in the vicinity of the KSL phase [50, 51]. This extension leads to the Kitaev-Heisenberg model, described by the Hamiltonian

$$H = K \sum_{\gamma \in \langle i, j \rangle} S_i^\gamma S_j^\gamma + J \sum_{\langle i, j \rangle} \mathbf{S}_i \cdot \mathbf{S}_j, \quad (2)$$

where $\gamma = x, y$ or z depending on the specific bond and $\mathbf{S}_i = (S_i^x, S_i^y, S_i^z)^T$, with the S_i^α being the spin operators acting on the i -th lattice site. The first term in the Hamiltonian represents the bond-dependent Kitaev interactions with coupling constant K while the second one is the conventional isotropic Heisenberg interaction with coupling constant J . This model has been suggested to describe iridium oxides such as Li_2IrO_3 and Na_2IrO_3 [36, 37]. The fact that the Kitaev-Heisenberg model can describe real materials with promising technological applications underscores the importance of understanding its behavior at large scales.

The Kitaev-Heisenberg model, like the original Kitaev model, was originally studied on a honeycomb lattice [36]. More recently, however, it has been shown that the Kitaev-Heisenberg model on a two-leg ladder lattice presents a phase diagram that is very similar to its honeycomb counterpart [22, 49].

Here we will focus on the $S = \frac{1}{2}$ Kitaev-Heisenberg

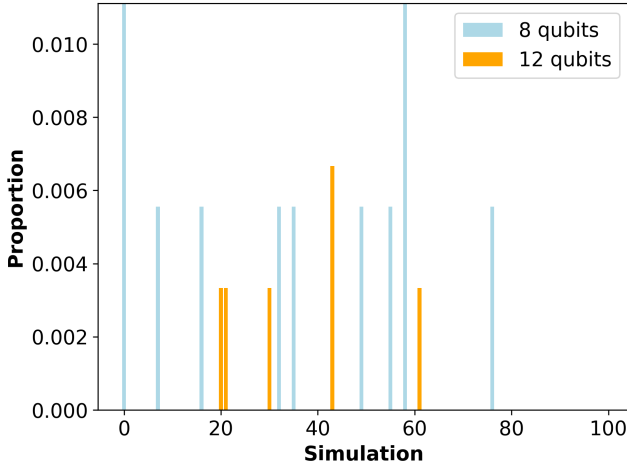


FIG. 4. The x-axis represents the i -th simulation, ranging from 1 to 100, and the y-axis shows the failure proportion ρ_{fail} considering the Kitaev-Heisenberg model. Similar results hold for the ANNNI model.

model on the two-legged ladder depicted in Fig. 2. In this case, the Hamiltonian in Eq. (2) can be decomposed as [49]

$$\begin{aligned}
 H = & K \sum_{i=1}^{L/2} \left(S_{2i-1,1}^x S_{2i,1}^x + S_{2i-1,1}^y S_{2i,1}^y \right) + J \sum_{i=1}^L \mathbf{S}_{i,1} \cdot \mathbf{S}_{i+1,1} \\
 & + K \sum_{i=1}^{L/2} \left(S_{2i,2}^x S_{2i+1,2}^x + S_{2i,2}^y S_{2i+1,2}^y \right) + J \sum_{i=1}^L \mathbf{S}_{i,2} \cdot \mathbf{S}_{i+1,2} \\
 & + K \sum_{i=1}^L S_{i,1}^z S_{i,2}^z + J \sum_{i=1}^L \mathbf{S}_{i,1} \cdot \mathbf{S}_{i,2},
 \end{aligned} \quad (3)$$

where the $S_{i,j}^\alpha$ are the spin operators acting on the i -th spin on the j -th leg of the ladder and L is the number of spins on each leg, making $N = 2L$ the total number of spins in the system.

The coupling constants for the Kitaev-Heisenberg model can be parameterized as functions of a parameter ϕ , with $K = \sin \phi$ and $J = \cos \phi$. Varying the value of ϕ reveals six different phases: four ordered phases and two spin liquid phases. They can be classified as follows [49]:

1. A rung-singlet (RS) phase for $-0.3\pi \leq \phi \leq 0.48\pi$, a trivial phase without magnetic order, where the unique ground state is adiabatically connected to a product of singlets on the rungs;
2. An antiferromagnetic Kitaev spin liquid (AFK) phase for $0.48\pi < \phi < 0.53\pi$. This corresponds to a narrow region around the pure Kitaev limit at $\phi = \frac{\pi}{2}$, where $J = 0$ and $K = 1$;
3. The zigzag (ZZ) phase (named after its analog phase in the honeycomb lattice) for $0.53\pi \leq \phi <$

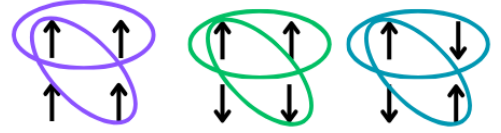


FIG. 5. Pictorial representation of neighbors and diagonal pairwise correlations for a states in different phases of a fictitious system

0.8π . This phase has ferromagnetic order on each leg, but the magnetization has opposite signs on different legs;

4. A ferromagnetic (FM) phase for $0.8\pi \leq \phi < 1.37\pi$, in the region around $\phi = \pi$, where $J = -1$ and $K = 0$ ensure ferromagnetic Heisenberg interactions between the spins;
5. A ferromagnetic Kitaev spin liquid (FK) phase for $1.37\pi \leq \phi \leq 1.57\pi$, the region around $\phi = \frac{3\pi}{2}$, where $J = 0$ and $K = -1$. Interestingly, this spin liquid phase is significantly wider than its antiferromagnetic counterpart;
6. The stripy (ST) phase for $1.57\pi < \phi < 1.7\pi$, with long-range antiferromagnetic order along each leg but ferromagnetic correlations between spins on the same rung.

The phases of the Kitaev-Heisenberg model described above are shown in Figure 3.

An interesting point to note about the AFK and FK spin liquid phases is that, although they do not present long-range order, they can be associated with near-unity expectation values for plaquette operators related to the flux of an emergent \mathbb{Z}_2 gauge field [33]. On the two-leg ladder, we consider the six-site plaquette operator given by [49]

$$\mathcal{O}_{\text{Plaquette}} = S_1^x S_2^y S_3^z S_4^x S_5^y S_6^z, \quad (4)$$

for the sites chosen as shown in Fig. 2. Strictly speaking, the expectation value of this plaquette operator does not qualify as an order parameter because it varies smoothly across the transitions out of the KSL phases. However, it can be calculated more easily than the string order parameter used in [22], with negligible finite-size effects, and drops rapidly in the long-range ordered phases [49].

The plaquette operators, as well as the two-point correlation functions between spins in the ladder, are the observables that we will estimate using classical shadows, which will then serve as the input data for identifying the different phases with a machine learning algorithm.

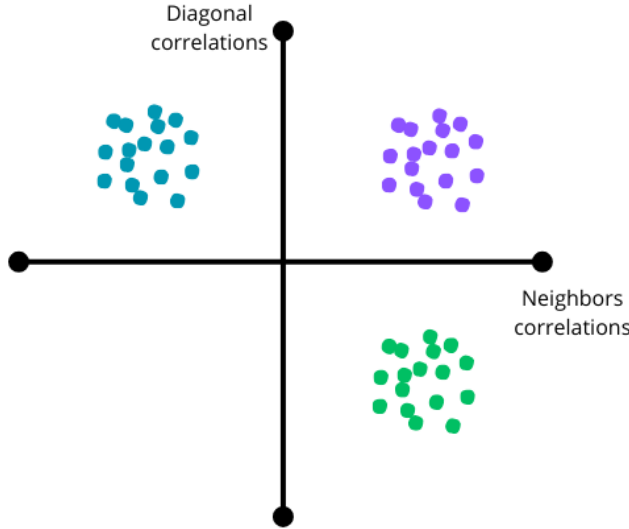


FIG. 6. Pairwise correlations for a fictional system with three distinct phases

III. AN OVERVIEW OF THE CLASSICAL SHADOWS METHOD

The classical shadows procedure involves preparing a state, applying a randomly selected set of unitaries $\rho \rightarrow U\rho U^\dagger$, followed by measurements on all qubits in the computational basis, which we refer to as a "snapshot." Subsequently, we store the n -bit measurement outcome $|\hat{b}_j\rangle \in \{0,1\}^n$ in classical memory and reconstruct ρ via a quantum channel \mathcal{M} , which depends on the chosen ensemble of unitaries. Repeating this procedure T times results in an array of T independent classical snapshots of ρ we can construct an array referred to as the classical shadows of ρ and given by

$$S(\rho; T) = \left\{ \hat{\rho}_1 = \mathcal{M}^{-1} \left(U_1^\dagger |\hat{b}_1\rangle \langle \hat{b}_1| U_1 \right), \right. \\ \left. \dots, \hat{\rho}_T = \mathcal{M}^{-1} \left(U_T^\dagger |\hat{b}_T\rangle \langle \hat{b}_T| U_T \right) \right\}. \quad (5)$$

In this work, we choose the random unitaries from the ensemble of Pauli unitaries, which allows us to perform the reconstruction of the state ρ as the average of $\hat{\rho}^m$ defined as

$$\hat{\rho}^m = \bigotimes_{j=1}^n \left(3(U_j^m)^\dagger |\hat{b}_j^m\rangle \langle \hat{b}_j^m| U_j^m - \mathbb{I} \right), \quad (6)$$

where U_j^m and $|\hat{b}_j^m\rangle$ represent the unitary acting on the j -th qubit and the outcome corresponding to the m -th measurement, respectively. With the classical shadows at hand, we can estimate linear functions using the expression

$$\hat{o} = \frac{1}{T} \sum_{m=1}^T \text{tr}(O \hat{\rho}^{(m)}), \quad (7)$$

where O is an operator acting on the system. In the case of Pauli unitaries, the number of snapshots increases logarithmically with the number of operators and exponentially with the locality of the operator, as stated in [5]. The number T of random Pauli measurements required to estimate a given observable with error ϵ is proportional to

$$T \propto \frac{\log(M) \cdot 3^l}{\epsilon^2}, \quad (8)$$

where M represents the number of operators to be estimated, l denotes the locality of the set of operators to be estimated, and ϵ is the error bound, which is defined as $|\hat{o}_i - \text{tr}(O_i \rho)| \leq \epsilon$. As discussed in [5], a probability of failure is expected, and the expected number of failures can be computed using the shadow norm.

Instead of evaluating the shadow norm, in this work, we fix the proportionality constant in Eq. (8) based on numerical simulations. For this purpose, we set $\epsilon = 0.1$ and run the circuit that prepares the ANNNI and Kitaev-Heisenberg ground state for systems of 8 and 12 qubits, performing 100 trials to estimate the expectation values, tracking the number of errors in each simulation and analyzing how this number evolves with the system size. Since the number of pairwise correlations grows with the number of qubits, to allow for a fair comparison we consider the error proportion defined as

$$\rho_{\text{fail}} = \frac{N_{\text{fail}}}{N_{\text{total}}}, \quad (9)$$

where N_{fail} is the number of operators estimated outside the error margin and N_{total} is the total number of estimated expectation values. The numerical simulations in Fig. 4 show that setting the proportional constant to 4 keeps the number of failures low enough and maintains a small number of measurements. Thus, in this work, the number of measurements is given by (setting $l = 2$)

$$T = \frac{36 \log(M)}{\epsilon^2}. \quad (10)$$

IV. PERFORMING THE FEATURE SELECTION

Selecting the right data to collect is as crucial as obtaining them, as this decision directly influences the success of the analysis. While all information is encoded in the state vector describing the quantum system, extracting it through state tomography is exponentially expensive in terms of both measurements and data processing. This raises an important question: given the ground state of a Hamiltonian, how can

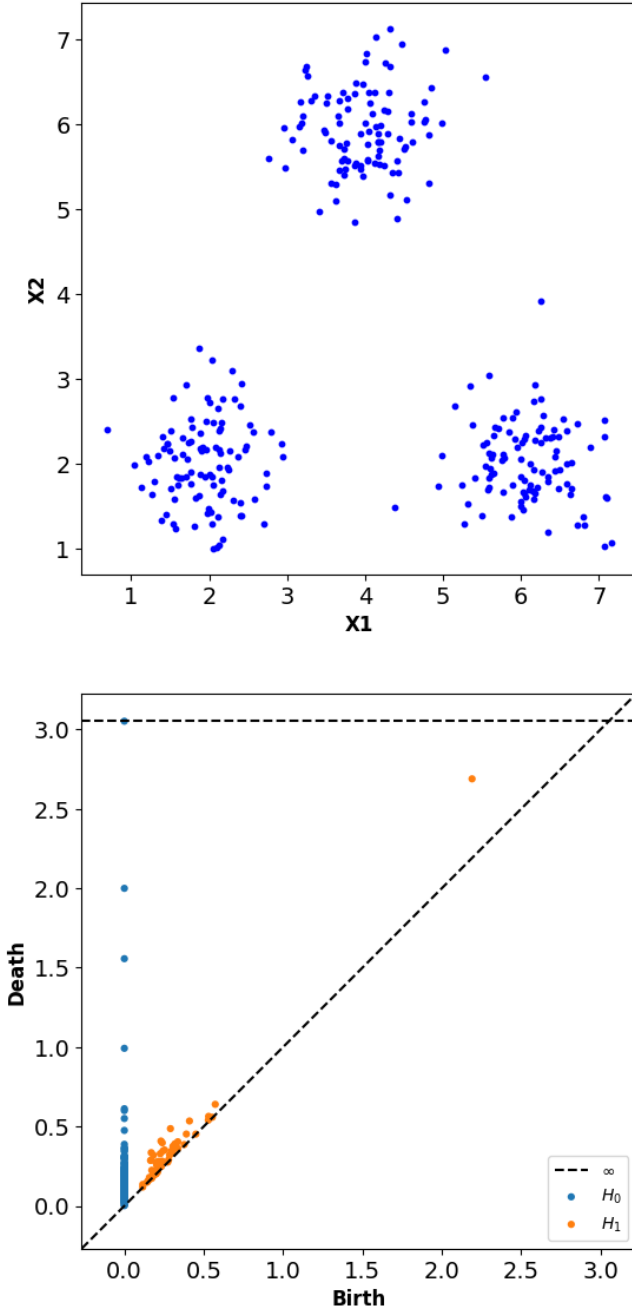


FIG. 7. Top panel: Spatial distribution of three Gaussian clusters. Bottom panel: Corresponding persistence diagram highlighting the identified topological features.

we extract meaningful information about the quantum phase of this state without the need to fully reconstruct it?

To illustrate this, consider the qualitative example shown in Figure 5. In this toy model, pairwise correlations between neighboring spins are sufficient to clearly indicate different phases. Specifically, for ordered systems where correlations are well defined,

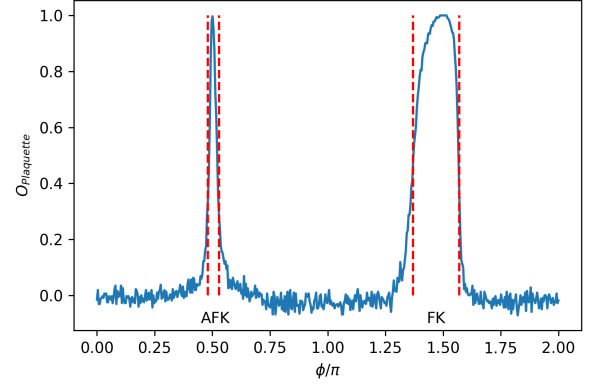


FIG. 8. Visualization of the expectation value of the plaquette operator in the Kitaev-Heisenberg model, see Eq. (8) and Fig. 2, for different values of the parameter ϕ , obtained by applying the derandomized classical shadows protocol to a Kitaev-Heisenberg ladder of $N = 2L = 12$ spins. The dashed lines are the KSL phase boundary results from Ref. [49].

the expectation values form distinct clusters that can be easily identified. As a result, clustering algorithms such as K-means can efficiently group these values and thereby distinguish the corresponding phases, as visually demonstrated in Figure 6.

A complementary approach to analyzing these clusters is provided by Topological Data Analysis (TDA), specifically through persistent homology. One of the main challenges when working with high-dimensional data is developing an intuitive understanding of its underlying structure. Persistent homology offers a qualitative method to capture the topological features of the data. In simple terms, persistent homology is constructed through a filtration process that generates k -simplices [52]. These k -simplices can be classified into (H_0) (connected components), (H_1) (structures with holes), (H_2) (cavities). As the filtration progresses, an increasing parameter ϵ governs the appearance and disappearance of these k -simplices, enabling the construction of a birth-death diagram [53]. These diagrams offer valuable insights into how homologies persist throughout the dataset, revealing its topological characteristics. For an illustration of these concepts, see Figure 7.

In Figure 7, three H_0 structures persist throughout the filtration process. Intuitively, the points further from the diagonal represent longer intervals associated with topological features that persist for a significant duration during the filtration. These points are considered to have high persistence and are typically interpreted as important topological features, while points near the diagonal are regarded as noise in

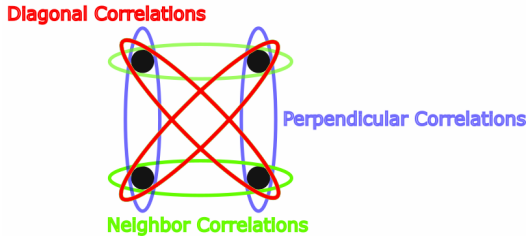


FIG. 9. Quadrant correlations on the Kitaev-Heisenberg ladder. For each set of four neighboring spins, we calculate the two-point correlators between each pair, ignoring correlations between spins separated by larger distances.

the data. If the clusters are too close together, persistent homology may struggle to effectively capture the clustering structure. Nevertheless, the information provided by the data can still be valuable from a qualitative perspective, as will be demonstrated in the case of the Kitaev-Heisenberg model.

A. Feature selection in the ANNNI model

Previous studies of the ANNNI model [45] have shown that the characterization of its main phases can be achieved taking as input the pairwise expectation values given by $\langle \lambda_0 | S_i^\alpha S_j^\alpha | \lambda_0 \rangle$, where $\alpha = x, y, z$, and $|\lambda_0\rangle$ represents a ground state of the ANNNI model for given values of the parameters g and k . In the first study to classify ANNNI phases using machine learning [45], all $N(N-1)$ pairwise correlators were used, resulting in a quadratic number of observables. However, as N increases, this approach risks introducing unnecessary computational complexity and adding redundant or noisy data, which can impair the accuracy of the algorithm in identifying phases. This challenge is especially relevant for algorithms implemented on quantum hardware, where limitations in qubit quality and quantity necessitate careful feature selection [46]. Based on this reasoning, we have reduced the number of correlators to just those involving NN and NNN sites, which, as will be shown, are already enough to provide a precise characterization of the gapped phases of the ANNNI model.

With this simplification, the number of two-local observables to be estimated for each state is given by $N_O = 3(2N-3)$, which scales linearly with the number of qubits. Consequently, the number of snapshots we need to perform using classical shadows is very efficient and given by

$$T = \frac{36 \log(6N-6)}{\epsilon^2}. \quad (11)$$

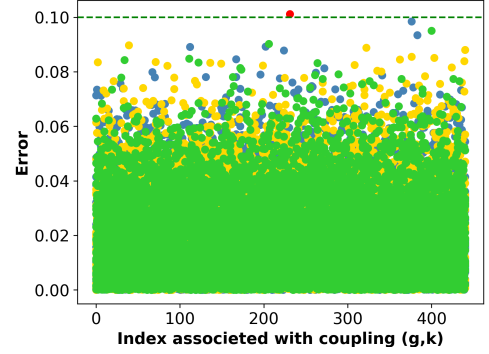


FIG. 10. Estimation of pairwise correlators for different spin directions and couplings. The horizontal axis represent different values of the couplings (g, κ) . The vertical axis is the margin of error ϵ . Each color represents a distinct spin direction: blue for X , yellow for Y and green for Z ; red points indicate estimates that fall outside the expected bounds

B. Feature selection in the Kitaev-Heisenberg model

As described in Sec. II B, the Kitaev-Heisenberg model exhibits two KSL phases as well as trivial and symmetry-breaking phases. It is thus crucial to differentiate between these phases to achieve more effective clustering. To classify these phases, we can compute the expected value of the plaquette operator using the derandomized classical shadows protocol, which is particularly well-suited for this analysis [54]. The results we present from now on refer to an $N = 2L = 12$ spin Kitaev-Heisenberg ladder.

As illustrated in Fig. 8, the plaquette operator acquires a nonzero expectation value of order unity inside the KSL phases. One can clearly observe a region around $\phi = 0.5\pi$ and a larger region around $\phi = 1.5\pi$ where the values deviate from zero. This allows us to distinguish between the spin liquid and ordered phases across the ϕ domain.

For the ordered phases, we need to choose which types of correlations to examine, for the same reasons discussed previously. Here, we will focus on the “quadrant correlations” shown in Fig. 9. This set includes correlations between NN spins on the same rung and on the each leg, as well as NNN spins along the diagonals throughout the ladder of length $N/2$. The number of observables to be estimated for each value of ϕ is given by $N_O = 3N-6$, resulting in a required number of snapshots given by

$$T = \frac{36 \log(3N-6)}{\epsilon^2}. \quad (12)$$

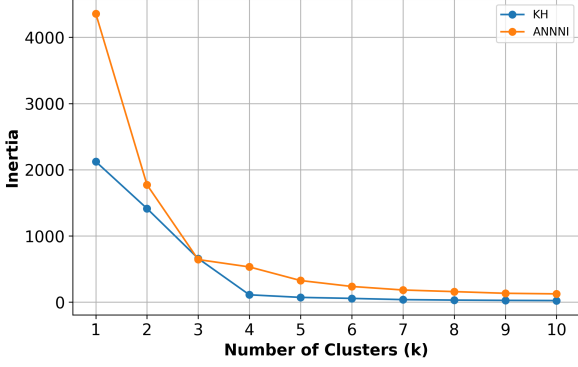


FIG. 11. Elbow curve for the ANNNI and Kitaev-Heisenberg model training data used to determine the optimal number of clusters for the K-Means algorithm. The curve shows the relationship between the number of clusters (k) and the sum of squared distances or inertia.

V. MACHINE LEARNING PHASE TRANSITIONS

A. The ANNNI model

As discussed in Sec. II, the ANNNI model exhibits four distinct phases, characterized by three phase transitions. These transitions can be identified using the K-Means algorithm, fed with pairwise correlations of the ground states for k, g couplings varying within the interval $[0, 1]$. We used Eq. (11) to compute the number of snapshots required to estimate the pairwise correlations with randomized measurements with a margin of error of 0.1 for each pair of k, g couplings. The results are presented in Fig. 10. Only one of the estimations overshoots the bound. However, as discussed in [5], some probability of failure is expected. In this way, the classical shadow algorithm performs as expected, regardless of spin component or couplings.

With the data at hand, it is necessary to evaluate its structure to determine the optimal number of clusters for the K-Means algorithm. While several techniques are available for this evaluation, we opted to use the Elbow method [55], for which the "elbow" point indicates the best balance between variance explained and model complexity. The results are presented in Fig. 11, showing the inertia values for different numbers of clusters, which is crucial for deciding how many clusters to select before running the K-Means algorithm. It is evident that after 4 clusters, the inertia decreases more slowly compared to the interval between 0 and 4 clusters. Following the approach in [45], we run the K-Means algorithm for 3 clusters, thereby leaving the floating phase aside.

This approach allows us to obtain the phase diagram for the ANNNI model, presented in Fig. 12, considering

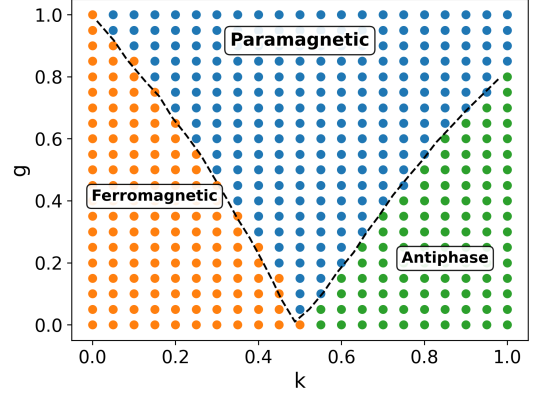


FIG. 12. Phase diagram of the ANNNI model for 12 qubits, where each color represents a distinct cluster corresponding to a different phase. The x-axis represents the coupling constant k , while the y-axis represents g , which affects the transverse field. The dashed black line represents the known approximation curves (see Ref. [45] for more details), which serve as our benchmark for comparison.

the Hamiltonian for 12 qubits. The result displays good agreement with the phase diagram obtained with much more numerical effort for larger system sizes [31]. We accurately determine the Ising transition between ordered (ferromagnetic) and disordered (paramagnetic) phases. The boundary between the paramagnetic phase and the antiphase falls in the region where we would expect to find the intervening gapless floating phase, which is not detected within this approach based on correlations for relatively small chains.

B. The Kitaev-Heisenberg model

As explained in Sec. IV B, the spin liquid phases of the Kitaev-Heisenberg models can be identified by estimating the plaquette operators using the derandomized classical shadows protocol. For the ordered phases, we employed a method similar to the one used for the ANNNI model, simulating states and estimating pairwise correlators via the classical shadows protocol. The results of the pairwise correlation estimations for the ordered phases are presented in Fig. 13. With the pairwise correlations well estimated, the next step is to determine the number of clusters present in the ordering phase data. As shown in Fig. 11, it is clear that the pairwise correlation data reveal four distinct groups, suggesting the existence of four ordered phases, as discussed in Section II. By combining the domain ϕ of the spin liquid phases, identified through the plaquette operators, with the domain partitioned into clusters via K-means, we

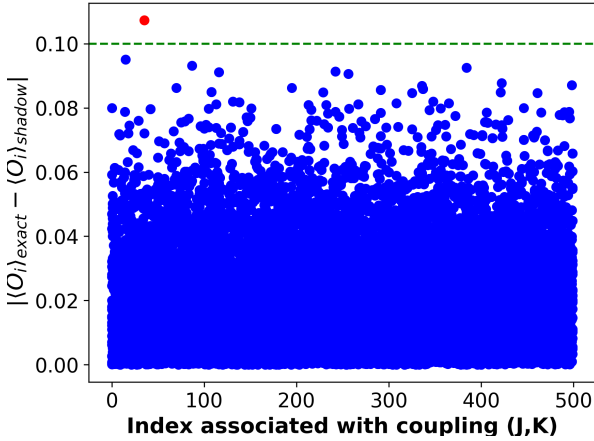


FIG. 13. Estimation of pairwise correlators for different couplings. The horizontal axis represents different values of the couplings (J, K) , and the vertical axis represents the margin of error $\epsilon = 0.1$. The red point indicates the correlation that falls outside the error bound, and the blue points represent the correlation estimations that respect the stipulated bound.

construct the phase diagram shown in Fig. 14.

The dots in the diagram represent the transition points between different phases in the thermodynamic limit. Notably, the transition between the zigzag and ferromagnetic phases appears less precise, while the transition from the stripy to the rung-singlet phase is much more accurate. This discrepancy arises because, with a limited number of qubits, the correlations between the zigzag and ferromagnetic phases become quite similar, making them harder to distinguish. To further explore this observation, we apply Principal Component Analysis (PCA) [56] to the pairwise correlation data of the Kitaev-Heisenberg model. PCA is a statistical method that transforms the original dataset, which may include correlated variables, into a new set of uncorrelated variables called principal components. These components are ranked by the amount of variance they capture, with the first few components accounting for the most significant variations in the system. In our analysis, we projected the results onto the first and second principal components. The outcome is shown in Fig. 15.

Except for the zigzag and ferromagnetic phases, the reduction of pairwise correlations of ordered phases into two principal components forms distinct groups, reflecting the different phases of the model. Furthermore, we can refer to the diagram of birth and death of persistence homologies in Fig. 16 and identify which topological features are important, as discussed in IV. For additional details, we recommend consulting [52]. As can be seen, we identify four

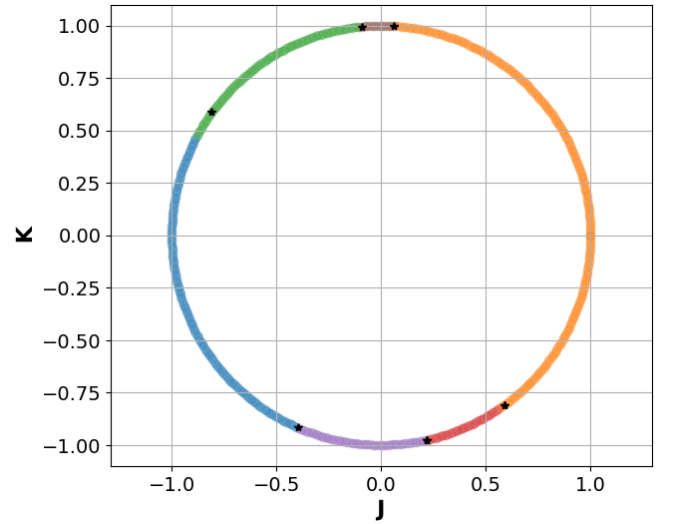


FIG. 14. Phase diagram of the Kitaev-Heisenberg model obtained from classical shadows for a ladder with 12 qubits. Each color represents a different phase. The black points represent the transition between these phases extracted from the phase diagram in Fig. 3.

structures (Ho), indicating the presence of four clusters in these data points. The persistence diagram and PCA support the results obtained via the K-means algorithm, highlighting that the difficulty in pinpointing the exact transition between the zigzag and ferromagnetic phases arises from the weakly defined correlations of these phases when dealing with a small number of qubits. However, as the number of qubits increases, these correlations become more distinct. Consequently, we expect the K-means algorithm to identify the transitions with more precision.

VI. DISCUSSION

This paper presents a quantum-classical pipeline for analyzing the phase diagram and phase transitions of quantum Hamiltonians. Using the ANNNI and Kitaev-Heisenberg models as benchmarks, we demonstrate how combining quantum computing with classical machine learning (ML) methods enables both qualitative and quantitative characterization of the complex phases in these Hamiltonians. We begin by showing how pairwise correlations and plaquette operators can be efficiently estimated using the classical shadows protocol. These estimates are highly consistent, with errors well below 1% for both models, underscoring the effectiveness of the protocol in generating reliable data from quantum measurement that then can be fed into classical ML models. Next, we explore how K-means clustering, a classical ML

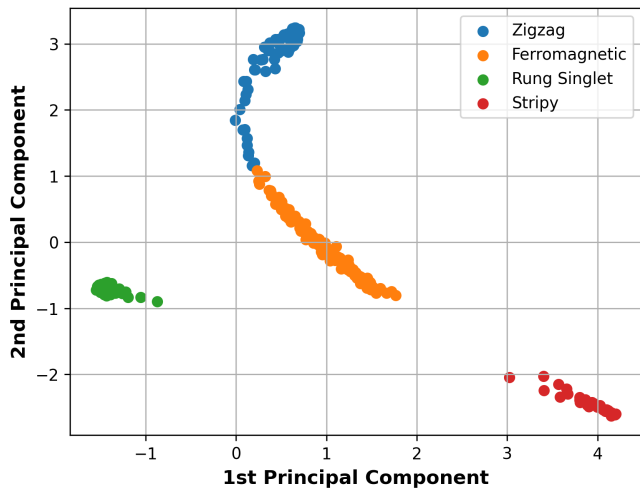


FIG. 15. The principal component analyses of pairwise correlations Kitaev-Heisenberg Model for 12 qubits, the differts collors represents the clusters obtained by the K-means algorithm.

algorithm, can process this data to accurately predict the three main phases (ferromagnetic, paramagnetic, and clustered antiphase/floating) of the ANNNI model and, with reasonable precision, recover the four ordered phases of the Kitaev-Heisenberg model (zigzag, ferromagnetic, stripy, and rung-singlet). While the results for the transition between the zigzag and ferromagnetic phases are less well-defined for a 12-qubit system, it is expected that increasing the lattice size will improve the precision in witnessing these transitions.

Despite the significant challenges inherent in quantum machine learning pipelines, such as barren plateaus and local minima, our results reinforce that a hybrid quantum-classical approach can still be genuinely useful, even with a limited number of qubits and we hope to motivate further investigation in Hamiltonian models of increasing number of qubits and complexity.

VII. ACKNOWLEDGEMENTS

We thank Richard Kueng for the inspiring lectures “The randomized measurement toolbox” given in Natal

and during the Paraty Quantum Information School that motivated the development of this work. We also thank the High Performance Computing Center (NPAD/UFRN) for providing computational resources. LM and TP acknowledge Marco Cerezo for fruitful conversations during the Second Quantum Computing School at ICTP-SAIFR. LM also thanks Pedro Alcantra for the productive discussions at IFSC-USP. DOSP

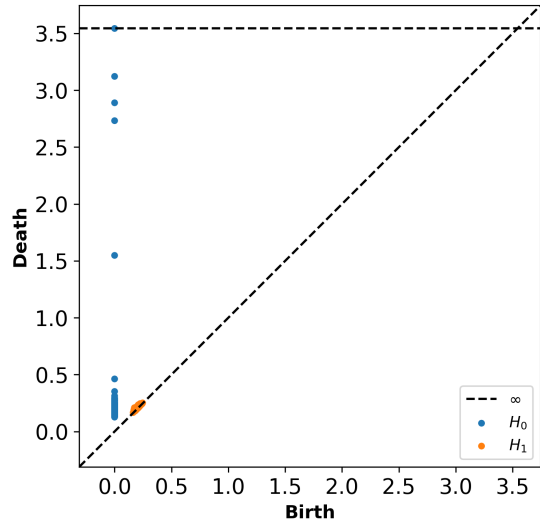


FIG. 16. Persistence Diagram for pairwise correlations estimated via classical shadows for 12 qubits

acknowledges the support by the Brazilian funding agencies CNPq (Grants No. 304891/2022-3 and No. 402074/2023-8), FAPESP (Grant No. 2017/03727-0 and No. 2023/03562-1) and the Brazilian National Institute of Science and Technology of Quantum Information (INCT/IQ). RC acknowledges the Simons Foundation (Grant Number 1023171, RC), the Brazilian National Council for Scientific and Technological Development (CNPq, Grant No.307295/2020-6 and 403181/2024-0) and the Otto Moensted Foundation visiting professorship. RGP acknowledges the Simons Foundation (Grant Number 1023171, RGP) and the Brazilian National Council for Scientific and Technological Development (CNPq, Grant No. 309569/2022-2 and 404274/2023-4). AC acknowledges partial financial support by the Alagoas State Research Agency (FAPEAL) (Grant No. APQ2022021000153), the CNPq (Grant No. 168785/2023-4) and by Centro de Competência do EDGE/UFAL.

[1] Giuseppe Carleo and Matthias Troyer. Solving the quantum many-body problem with artificial neural networks. *Science*, 355(6325):602–606, 2017.

[2] Giacomo Torlai, Guglielmo Mazzola, Juan Carrasquilla, Matthias Troyer, Roger Melko, and Giuseppe Carleo. Neural-network quantum state tomography. *Nature physics*, 14(5):447–450, 2018.

- [3] Giuseppe Carleo, Ignacio Cirac, Kyle Cranmer, Laurent Daudet, Maria Schuld, Naftali Tishby, Leslie Vogt-Maranto, and Lenka Zdeborová. Machine learning and the physical sciences. *Reviews of Modern Physics*, 91(4):045002, 2019.
- [4] Juan Carrasquilla. Machine learning for quantum matter. *Advances in Physics: X*, 5(1):1797528, 2020.
- [5] Hsin-Yuan Huang, Richard Kueng, and John Preskill. Predicting many properties of a quantum system from very few measurements. *Nature Physics*, 16(10):1050–1057, 2020.
- [6] Juan Carrasquilla and Roger G Melko. Machine learning phases of matter. *Nature Physics*, 13(5):431–434, 2017.
- [7] Xiao-Yu Dong, Frank Pollmann, and Xue-Feng Zhang. Machine learning of quantum phase transitions. *Phys. Rev. B*, 99:121104, Mar 2019.
- [8] Alexander Lidiak and Zhexuan Gong. Unsupervised machine learning of quantum phase transitions using diffusion maps. *Phys. Rev. Lett.*, 125:225701, Nov 2020.
- [9] Peter Broecker, Juan Carrasquilla, Roger G Melko, and Simon Trebst. Machine learning quantum phases of matter beyond the fermion sign problem. *Scientific reports*, 7(1):8823, 2017.
- [10] Joaquin F Rodriguez-Nieva and Mathias S Scheurer. Identifying topological order through unsupervised machine learning. *Nature Physics*, 15(8):790–795, 2019.
- [11] Xiao-Yu Dong, Frank Pollmann, and Xue-Feng Zhang. Machine learning of quantum phase transitions. *Physical Review B*, 99(12):121104, 2019.
- [12] AV Uvarov, AS Kardashin, and Jacob D Biamonte. Machine learning phase transitions with a quantum processor. *Physical Review A*, 102(1):012415, 2020.
- [13] Flavio Noronha, Askery Canabarro, Rafael Chaves, and Rodrigo G Pereira. Predicting topological invariants and unconventional superconducting pairing from density of states and machine learning. *arXiv preprint arXiv:2408.16499*, 2024.
- [14] Yanming Che, Clemens Gneiting, Tao Liu, and Franco Nori. Topological quantum phase transitions retrieved through unsupervised machine learning. *Phys. Rev. B*, 102:134213, Oct 2020.
- [15] William MC Foulkes, Lubos Mitas, RJ Needs, and Guna Rajagopal. Quantum monte carlo simulations of solids. *Reviews of Modern Physics*, 73(1):33, 2001.
- [16] Marcus Cramer, Martin B Plenio, Steven T Flammia, Rolando Somma, David Gross, Stephen D Bartlett, Olivier Landon-Cardinal, David Poulin, and Yi-Kai Liu. Efficient quantum state tomography. *Nature communications*, 1(1):149, 2010.
- [17] Marco Cerezo, Guillaume Verdon, Hsin-Yuan Huang, Lukasz Cincio, and Patrick J Coles. Challenges and opportunities in quantum machine learning. *Nature Computational Science*, 2(9):567–576, 2022.
- [18] Lennart Bittel and Martin Kliesch. Training variational quantum algorithms is np-hard. *Physical review letters*, 127(12):120502, 2021.
- [19] Hsin-Yuan Huang, Michael Broughton, Masoud Mohseni, Ryan Babbush, Sergio Boixo, Hartmut Neven, and Jarrod R McClean. Power of data in quantum machine learning. *Nature communications*, 12(1):2631, 2021.
- [20] Scott Aaronson. Shadow tomography of quantum states. In *Proceedings of the 50th annual ACM SIGACT symposium on theory of computing*, pages 325–338, 2018.
- [21] Walter Selke. The annni model—theoretical analysis and experimental application. *Physics Reports*, 170(4):213–264, 1988.
- [22] Andrei Catuneanu, Erik S. Sørensen, and Hae-Young Kee. Nonlocal string order parameter in the $S = \frac{1}{2}$ Kitaev-Heisenberg ladder. *Phys. Rev. B*, 99:195112, May 2019.
- [23] Xiao-Yong Feng, Guang-Ming Zhang, and Tao Xiang. Topological characterization of quantum phase transitions in a spin-1/2 model. *Phys. Rev. Lett.*, 98:087204, Feb 2007.
- [24] Hidenori Takagi, Tomohiro Takayama, George Jackeli, Giniyat Khaliullin, and Stephen E. Nagler. Concept and realization of Kitaev quantum spin liquids. *Nature Reviews Physics*, 1(4):264–280, 2019.
- [25] Stuart Lloyd. Least squares quantization in pcm. *IEEE transactions on information theory*, 28(2):129–137, 1982.
- [26] R. J. Elliott. Phenomenological discussion of magnetic ordering in the heavy rare-earth metals. *Phys. Rev.*, 124:346–353, Oct 1961.
- [27] J. Villain and P. Bak. Two-dimensional ising model with competing interactions : floating phase, walls and dislocations. *Journal de Physique*, 42(5):657–668, 1981.
- [28] D Allen, P Azaria, and P Lecheminant. A two-leg quantum ising ladder: a bosonization study of the ANNNI model. *Journal of Physics A: Mathematical and General*, 34(21):L305–L310, may 2001.
- [29] Heiko Rieger and Genadi Uimin. The one-dimensional ANNNI model in a transverse field: analytic and numerical study of effective hamiltonians. *Zeitschrift für Physik B Condensed Matter*, 101(4):597–611, dec 1996.
- [30] Paulo R. Colares Guimarães, João A. Plascak, Francisco C. Sá Barreto, and João Florencio. Quantum phase transitions in the one-dimensional transverse ising model with second-neighbor interactions. *Phys. Rev. B*, 66:064413, Aug 2002.
- [31] Matteo Beccaria, Massimo Campostrini, and Alessandra Feo. Evidence for a floating phase of the transverse annni model at high frustration. *Phys. Rev. B*, 76:094410, Sep 2007.
- [32] Adam Nagy. Exploring phase transitions by finite-entanglement scaling of MPS in the 1d ANNNI model. *New Journal of Physics*, 13(2):023015, feb 2011.
- [33] Alexei Kitaev. Anyons in an exactly solved model and beyond. *Annals of Physics*, 321(1):2–111, 2006. January Special Issue.
- [34] Rodrigo G. Pereira and Reinhold Egger. Electrical Access to Ising Anyons in Kitaev Spin Liquids. *Phys. Rev. Lett.*, 125:227202, Nov 2020.
- [35] A.Yu. Kitaev. Fault-tolerant quantum computation by anyons. *Annals of Physics*, 303(1):2–30, 2003.
- [36] Jiří Chaloupka, George Jackeli, and Giniyat Khaliullin. Kitaev-Heisenberg Model on a Honeycomb Lattice: Possible Exotic Phases in Iridium Oxides $A_2\text{IrO}_3$. *Phys. Rev. Lett.*, 105:027204, Jul 2010.
- [37] Yogesh Singh, S. Manni, J. Reuther, T. Berlijn, R. Thomale, W. Ku, S. Trebst, and P. Gegenwart. Relevance of the Heisenberg-Kitaev Model for the Honeycomb Lattice

- Iridates $A_2\text{IrO}_3$. *Phys. Rev. Lett.*, 108:127203, Mar 2012.
- [38] M. Cea, M. Grossi, S. Monaco, E. Rico, L. Tagliacozzo, and S. Vallecorsa. Exploring the phase diagram of the quantum one-dimensional annni model, 2024.
 - [39] Walter Selke. The annni model — theoretical analysis and experimental application. *Physics Reports*, 170(4):213–264, 1988.
 - [40] Askery Canabarro, Felipe Fernandes Fanchini, André Luiz Malvezzi, Rodrigo Pereira, and Rafael Chaves. Unveiling phase transitions with machine learning. *Phys. Rev. B*, 100:045129, Jul 2019.
 - [41] J.-J. Wen, W. Tian, V. O. Garlea, S. M. Koohpayeh, T. M. McQueen, H.-F. Li, J.-Q. Yan, J. A. Rodriguez-Rivera, D. Vaknin, and C. L. Broholm. Disorder from order among anisotropic next-nearest-neighbor Ising spin chains in SrHo_2O_4 . *Phys. Rev. B*, 91:054424, Feb 2015.
 - [42] C. Karrasch and D. Schuricht. Dynamical phase transitions after quenches in nonintegrable models. *Phys. Rev. B*, 87:195104, May 2013.
 - [43] Fabian Hassler and Dirk Schuricht. Strongly interacting majorana modes in an array of josephson junctions. *New Journal of Physics*, 14(12):125018, dec 2012.
 - [44] A. Milsted, L. Seabra, I. C. Fulga, C. W. J. Beenakker, and E. Cobanera. Statistical translation invariance protects a topological insulator from interactions. *Phys. Rev. B*, 92:085139, Aug 2015.
 - [45] Askery Canabarro, Felipe Fernandes Fanchini, André Luiz Malvezzi, Rodrigo Pereira, and Rafael Chaves. Unveiling phase transitions with machine learning. *Physical Review B*, 100(4):045129, 2019.
 - [46] André J Ferreira-Martins, Leandro Silva, Alberto Palhares, Rodrigo Pereira, Diogo O Soares-Pinto, Rafael Chaves, and Askery Canabarro. Detecting quantum phase transitions in a frustrated spin chain via transfer learning of a quantum classifier algorithm. *Physical Review A*, 109(5):052623, 2024.
 - [47] Lucile Savary and Leon Balents. Quantum spin liquids: a review. *Rep. Prog. Phys.*, 80(1):016502, nov 2016.
 - [48] C. Broholm, R. J. Cava, S. A. Kivelson, D. G. Nocera, M. R. Norman, and T. Senthil. Quantum spin liquids. *Science*, 367(6475):eaay0668, 2020.
 - [49] Cliò Efthimia Agrapidis, Jeroen van den Brink, and Satoshi Nishimoto. Ground state and low-energy excitations of the Kitaev-Heisenberg two-leg ladder. *Phys. Rev. B*, 99:224418, Jun 2019.
 - [50] Jeffrey G. Rau, Eric Kin-Ho Lee, and Hae-Young Kee. Generic spin model for the honeycomb iridates beyond the kitaev limit. *Phys. Rev. Lett.*, 112:077204, Feb 2014.
 - [51] Ioannis Rousochatzakis, Natalia B Perkins, Qiang Luo, and Hae-Young Kee. Beyond Kitaev physics in strong spin-orbit coupled magnets. *Rep. Prog. Phys.*, 87(2):026502, feb 2024.
 - [52] Frédéric Chazal and Bertrand Michel. An introduction to topological data analysis: fundamental and practical aspects for data scientists. *Frontiers in artificial intelligence*, 4:667963, 2021.
 - [53] Yueqi Cao, Prudence Leung, and Anthea Monod. k-means clustering for persistent homology. *Advances in Data Analysis and Classification*, pages 1–25, 2024.
 - [54] Hsin-Yuan Huang, Richard Kueng, and John Preskill. Efficient estimation of pauli observables by derandomization. *Physical review letters*, 127(3):030503, 2021.
 - [55] Muhammad Ali Syakur, B Khusnul Khotimah, EMS Rochman, and Budi Dwi Satoto. Integration k-means clustering method and elbow method for identification of the best customer profile cluster. In *IOP conference series: materials science and engineering*, volume 336, page 012017. IOP Publishing, 2018.
 - [56] Sam Roweis. Em algorithms for pca and spca. *Advances in neural information processing systems*, 10, 1997.